Research Square

Preprints are preliminary reports that have not undergone peer review.
They should not be considered conclusive, used to inform clinical practice,
or referenced by the media as validated information.

Spatiotemporal remodeling in the habenula marks the onset of depression

Manuel Mameli

manuel.mameli@unil.ch

The University of Lausanne https://orcid.org/0000-0002-0570-6964

Patricia Molina

The University of Lausanne

Denys Osypenko

The University of Lausanne

Josep Garnica Caparrós

University of Lausanne https://orcid.org/0000-0001-9493-1321

Quentin Amossé

The University of Lausanne https://orcid.org/0000-0002-5553-9594

Sarah Mondoloni

The University of Lausanne

Mauro Congiu

The University of Lausanne

Claudia Kathe

University of Lausanne https://orcid.org/0000-0001-6441-1755

Biological Sciences - Article

Keywords:

Posted Date: November 19th, 2025

DOI: https://doi.org/10.21203/rs.3.rs-7773881/v1

License: This work is licensed under a Creative Commons Attribution 4.0 International License.
Read Full License

Additional Declarations: There is **NO** Competing Interest.

Version of Record: A version of this preprint was published at Nature Neuroscience on October 19th, 2026. See the published version at https://doi.org/10.1038/s41593-026-02488-6.

Spatiotemporal remodeling in the habenula marks the onset of depression

Authors: Patricia Molina[1], Denys Osypenko[1], Josep Garnica[2,3], Quentin Amossé[1], Sarah Mondoloni[1], Mauro Congiu[1], Claudia Kathe[1], Manuel Mameli[1,4*]

Affiliations:

[1] The Department of Fundamental Neuroscience, The University of Lausanne 1005 Lausanne, Switzerland.

[2] Department of Oncology, Ludwig Institute for Cancer Research, Lausanne Branch, CHUV and University of Lausanne, 1011 Lausanne, Switzerland. AGORA Cancer Research Center, 1005, Lausanne, Switzerland.

[3] Swiss Institute of Bioinformatics, 1015 Lausanne, Switzerland.

[4] Inserm, UMR-S 839, 75005 Paris, France.

*Correspondence to: manuel.mameli@unil.ch

Chronic stress has lasting adverse consequences that can lead, over time, to depressive disorders[1-4] yet identifying the optimal timeframe for effective therapies remains an unmet challenge. Enhanced neuronal activity and disrupted aversion-encoding in lateral habenula (LHb) are important mediators of stress-related behavioral repercussions[5-10], although the precise timing of its contribution is not understood. Here, we identified an antidepressant-sensitive onset of stress consequences in mice, observable across multiple levels of biological complexity – behavioral, functional, and molecular. Using spatial transcriptomics[11,12], we generated a spatially-resolved molecular atlas of the LHb, revealing a topographically-organized and temporally-defined remodeling of gene expression in chronic stress. Longitudinal in vivo two-photon calcium imaging to survey the encoding properties of individual LHb neurons revealed progressively heightened excitatory responses to aversive stimuli. These neuronal adaptations were reversed by the antidepressant ketamine and mirrored both the progression of transcriptional changes as well as the emergence of depression-related behavioral phenotypes. Finally, both chemogenetically limiting LHb neuronal activity and administering ketamine at the onset of the remodeling processes exerted antidepressant effects. Together, these findings associate shared spatiotemporal signatures of LHb neuronal ensembles and genetic landscape with the onset of stress-induced depression-related states. This has implications for temporally tailoring therapeutical interventions in clinical practice.

One Sentence Summary: Spatially- and time-resolved remodeling in habenula for stress-driven depression.

Depression is characterized by alternating episodes of persistent low mood and diminished coping capacity, interspersed with periods of apparent wellness[1]. While antidepressant treatments are available, they are effective in only a fraction of individuals, partly due to challenges in timely diagnosis and treatment initiation[13-16]. This requires an understanding of the trajectories of the depressive state and their underlying mechanisms to ultimately tailor therapies within defined temporal windows[2,6,9].

In humans, repeated exposure to stressful events and the consequent prolonged elevation of stress mediators (e.g., cortisol) can lead to the emergence of depressive episodes[17-19]. Similarly, in rodents, paradigms that chronically elevate stress hormones, including protracted restraint, social defeat, or administration of corticosterone[2,5,20] recapitulate core behavioral features of human depression[8,20,21]. However, most research has focused on the consequences of prolonged stress exposure only at a late time point. This leaves a gap in understanding the temporal trajectories delineating the onset of depression-related behaviors (defined here as the onset of stress susceptibility) and its underlying mechanisms during chronic stress.

The lateral habenula (LHb) is a primary target of stressful events, with neurons in this structure activated by a wide range of stressors across various species[21-26]. In rodents, chronic stress perturbs gene expression, alters synaptic neurotransmission, and increases neuronal activity in the LHb, leading to behavioral signatures reminiscent of human depression[21,27-30]. Notably, once depression-related behaviors are established, various antidepressant treatments can normalize them by restoring physiological neuronal parameters in the LHb[8,31-34]. However, the temporal relationship between the onset of LHb adaptations and the emergence of depressive phenotypes remains poorly understood.

By leveraging recent advances in spatial transcriptomics[12], high-resolution in vivo imaging of deep brain structures[22,35], and behavioral phenotyping across chronic stress, we tested the hypothesis that a therapeutically-relevant onset exists for stress susceptibility when depression-related behaviors emerge.

Remodeling of a LHb molecular cartography in depression

The LHb exhibits molecular and functional diversity, features likely contributing to its territorially-distributed input-output organization as well as to stress-driven adaptations[23,36-39]. Whether the genetic landscape and its remodeling enable LHb neurons to regulate behavioral

responses to prolonged stress remains elusive. Chronic corticosterone (CORT; the principal rodent stress hormone) administration in rodents recapitulates aspects of the neuroendocrine response to prolonged stress and induces depression-related behaviors, providing a controlled model of chronic stress[2,40-42]. Thus, to study the repercussions of CORT accumulation over time and pinpoint the onset of stress susceptibility, independent cohorts of C57BL/6J mice were exposed (or not, baseline, *t*0) to CORT (0.10 mg/mL) in their drinking water at different regimens (1, 7, 21 days administration, *t*1, *t*7, *t*21, respectively; Fig. 1a).

We anticipated that charting transcriptional adaptations over time during stress accumulation would require first a cartography of the molecular organization within the LHb, which we addressed using high-throughput spatial transcriptomics technologies for mapping gene expression[11,12]. We sequenced 32 coronal sections containing the habenula (n = 4/cohort, 2 technical replicates each) yielding a median of 50 spots per habenular complex per section, and a median sequencing depth of 7'664 unique molecular identifiers (UMIs) and 3'844 detected genes per spot (Fig. 1a–b; Extended Data Fig. 1a). To enable comparisons across experimental conditions, we registered all the spots within the habenular complex and embedded them in a common coordinate framework (Fig. 1c). Unsupervised clustering of these spots identified two clusters (visualized using uniform manifold approximation and projection, UMAP; Fig. 1d) that expressed canonical marker genes of LHb (*Gap43,* lateral) and medial habenula (MHb, *Tac2,* medial), respectively. This, added to their and other marker genes' medio-lateral localization, enabled the accurate annotation of LHb territories for the subsequent analyses (Fig. 1d-f; Extended Data Fig. 1b)[23,39,43]. Spot-level analysis of LHb region revealed transcriptional profiles typical of neurons, glia, and other cell types based on established marker gene expression (Extended Data Fig. 1c)[23,39]. We then investigated whether spatial gene expression patterns varied within the LHb under baseline (*t*0) conditions. An unbiased analysis using axis regression on principal components (PC) revealed that medial-to-lateral positioning associated with transcriptional variability within the LHb territory (Extended Data Fig. 1d, e)[22,36,44]. We focused on genes with the highest loadings on PC1, which captured most of transcriptional variation along the mediolateral axis (Extended Data Fig. 1f). We mapped their expression across individual spots, which unmasked medial and lateral biases, a signature that similarly emerged in an independent Stereo-seq-based and spatially-resolved dataset[45] (Extended Data Fig. 1g, h). Notably, the top genes contributing to this mediolateral gradient were mainly expressed in neurons (Extended Data Fig. 1i). These spatial patterns guided the subdivision of the LHb into medial, central, and lateral subregions (Fig. 1f). Thus, this resulting

transcriptional atlas offers a molecular map of LHb subterritories, providing a foundation for investigating their remodeling in the context of stress susceptibility.

We then examined transcriptional changes across independent cohorts of mice at baseline (*t*0, no CORT) and after 1, 7, and 21 days of CORT exposure within the different LHb territories (medial, central, and lateral) (Fig. 1a, f). Pronounced transcriptional remodeling emerged at day 7 of CORT administration (*t*7) in all LHb subregions, as indicated by their shift from baseline, quantified using silhouette score in the PC space (visualized using UMAP) (Fig. 1g, h; Extended Data Fig. 1d). Notably, the extent of differentially expressed genes (DEG; CORT vs baseline) across CORT exposure was almost 3-fold larger in the LHb lateral domain compared to the central one (Fig. 1i, j). On the contrary, the LHb medial territory showed the least DEGs (Fig. 1j). These findings are consistent with previous reports causally linking depression-related states to spatially restricted (lateral) synaptic input adaptations in the LHb [4,27] and reveal a critical period for transcriptional remodeling within this structure.

To further characterize these transcriptional changes, we performed gene ontology (GO) enrichment analysis of the DEGs significantly altered within lateral LHb spots, identified as the subregion most affected by chronic CORT. CORT exposure led to changes in gene sets associated with neuronal function, including membrane potential, ion channel activity, and behavioral responses (Fig. 1k; Extended Data Table 1). Notably, amongst the CORT-sensitive DEGs, specific ones related to ion channels and synaptic function (*Slc24a2* and *Map1b*), were shared across stress paradigms (Extended Data Fig. 2a-b)[21,23]. Thus, transcriptional landscapes adapt within precise and behaviorally-relevant brain networks in depression[46,47].

Spatiotemporal dynamics of LHb neuronal activity across chronic CORT

Molecular fluctuations in the LHb associated with aversive experiences are temporally-matched by neuronal activity dynamics[23]. Given that gene expression within the LHb, particularly in its lateral domain, varied throughout CORT administration, we sought to longitudinally track single-cell neuronal activity. This enables assessing whether transcriptional and functional remodeling in LHb mark the same onset of stress susceptibility. To optimally design longitudinal imaging experiments in head-fixed animals (using airpuff as aversive stimulus), we examined aversion-related behavioral adaptations in mice subjected to chronic CORT. As shown with a variety of aversive stimuli[48,49], CORT reduced airpuff-induced escapes at *t*7 and *t*21 compared to control animals (EtOH 1% vehicle; Extended Data

Fig. 3a). Hence, we infused an adeno-associated viral construct encoding the Ca^{2+} indicator GCaMP8m (AAV_{DJ}-hSyn-GCaMP8m) into the LHb of C57BL/6J mice and then implanted a microendoscopic lens ~50 µm above the injection site, permitting optical access to LHb neurons (Fig. 2a). Calcium dynamics were measured *in vivo* with two-photon microscopy[22,35] within stable fields of view (FOV) in head-fixed mice exposed to unpredicted aversive airpuffs during recordings at baseline (*t*0) and after 1, 7, 14 and 21 days of CORT administration (*t*1 to *t*21; Fig. 2a, b).

We observed that, at *t*0, a subset of LHb neurons was excited by airpuffs, while others were either non-responsive or displayed reduced fluorescence[22,50] (Fig. 2b; Extended Data Fig. 3b–d). A larger fraction of excited neurons emerged after CORT administration along with an increased population response magnitude at CORT *t*21, compared to *t*0 and vehicle–administered group (Extended Data Fig. 3b–d). The average airpuff responses from each neuron at *t*0 and *t*21, in both vehicle and CORT mice, were then used to investigate whether neuronal subsets with distinct functional properties exist across CORT-driven stress accumulation. We utilized K-means clustering algorithm to identify six functional clusters that could be grouped into three major categories based on the airpuff-elicited neuronal responses at *t*0 (baseline) – increased (Bas. Up; cluster 1 and 2), non-changed (Bas. Null; cluster 3 and 4) and reduced (Bas. Down; cluster 5 and 6) fluorescence (Fig. 2c-e; Extended Data Fig. 3e). When inspecting clusters showing the largest change in airpuff response over the course of recordings (Clusters 3 and 5; Fig. 2d), the proportion of neurons belonging to these clusters was significantly higher in CORT-administered mice compared to vehicle (Fig. 2e). Notably, the temporal trajectories of airpuff responses across clusters during CORT treatment revealed cluster-specific plasticity and an onset of adaptations matching that of transcriptional changes (*t*7, Fig. 2f). This supports that stress remodels LHb neuronal responses[10] and suggests that chronic CORT exposure recruits selective neuronal ensembles within a defined timeframe, mirroring the temporal signatures of transcriptional remodeling.

Next, we examined whether, similarly to the transcriptional changes, the reorganization of neuronal responses was also spatially resolved. We collapsed all recorded FOVs containing LHb GCaMP8m-expressing neurons, aligned them with their respective Gradient Index (GRIN) lens edges and projected them onto an LHb anatomical mask (Extended Data Fig. 3f–h). This revealed that plasticity of airpuff responses across CORT administration was cluster-specific (affecting only cells initially non-responsive or inhibited by airpuff; Clusters 3-6), and

significantly larger in the lateral domains of the LHb with the onset at *t*7 CORT (Fig. 2g-i; Extended Data Fig. 3i–k). Thus, spatially-biased LHb neuronal activity dynamics temporally recapitulate gene expression variations in lateral LHb during CORT administration, further supporting the existence of an onset for stress susceptibility.

Antidepressant-purposed ketamine restores CORT-mediated LHb remodeling

We reasoned that if the onset of neuronal ensembles plasticity in LHb is a feature of chronic stress susceptibility and depression-related states, CORT-driven adaptations of airpuff responses across specific LHb cell clusters shall be sensitive to antidepressant strategies. To test this, we performed longitudinal two-photon imaging to analyze LHb neuronal activity at baseline (*t*0) and *t*7 of CORT exposure (as the onset of CORT-induced LHb remodeling) after administration of saline or the antidepressant ketamine [10 mg kg^{-1} body weight, i.p.][29,33] (Fig. 3a, Extended Data Fig. 4a). While CORT significantly increased airpuff-evoked excitation in saline-treated mice at *t7* (Fig. 3b; see also Fig. 2d, f), ketamine normalized population airpuff responses in CORT mice, similar to baseline levels, and significantly lower than in the saline–treated CORT group (Fig. 3b-d). We then applied the k-means clustering algorithm to embed the airpuff responses in ketamine- and saline-treated mice at *t*0 and *t7* into the previously identified six neuronal response types (Fig. 2c; Fig 3e, See Methods). Cluster analysis indicated that the effect of ketamine was driven by the decrease of population size of the CORT-sensitive cluster 3 mostly within the LHb lateral domains, while cluster 1 decreased in its representation and cluster 5 remained instead unaffected by treatment (Fig 3f-h; Extended Data Fig. 4b-e). Thus, these findings identify an early critical period in which CORT-induced spatiotemporal adaptations of selected LHb neuronal ensembles are sensitive to and reversible by the antidepressant ketamine.

Temporally-defined behavioral signatures of depression

Antidepressant treatments, including fast-acting agents like ketamine, lead to the remission of behavioral phenotypes in multiple animal models of stress susceptibility and depression[2,8,21,29,34,51]. Mechanistically, these effects are, at least in part, mediated via the blockade of NMDAR-dependent LHb neuronal burst firing, ultimately reducing the activity of LHb neurons[31,33]. However, the appropriate timing for treatment initiation remains debated for mood disorders, and it only starts long after symptoms are fully manifested[52]. Do behavioral adaptations follow a similar trajectory to LHb transcriptional and activity remodeling? To identify behavioral susceptibility to stress across time, we subjected independent cohorts of

mice to CORT (or vehicle) administration for 1, 7 or 21 days and quantified, for each animal, the levels of threat escapes, active coping, and self-caring behavior (i.e., grooming) (Fig. 4a, Extended Data Fig. 5a) – considered traits of stress-mediated depression-related states[5,21,53]. We then computed an integrated behavioral state for each animal by combining individual behavioral scores into a 3D phenotypic space. Mice administered with CORT for one day presented a behavioral state similar to vehicle-treated controls (Fig. 4b, c; Extended Data Fig. 5b). In contrast, divergent behavioral states emerged at day 7 and persisted until day 21, as shown by significant increase in clustering accuracy between CORT-treated mice and their respective controls (Fig. 4c). Notably, CORT repercussions on behavioral state were consistent across stress-associated phenotypes, as a similar trajectory was observed for the CORT-driven reduction in airpuff escapes (Extended Data Fig. 3a). Measures of locomotion, as well as the interaction with the threat before and after the task, remained stable across groups (Extended Data Fig. 5c-e). Finally, to test whether the proposed onset of stress susceptibility generalizes to other models of chronic stress, we conducted behavioral phenotyping in mice exposed to either 1, 7, or 21 days of repeated restraint stress, a commonly used stress paradigm in rodents[4,5], and found comparable behavioral trajectories (Extended Data Fig. 5f-h). Thus, depression-related behaviors emerge time-locked with a critical period of multilevel (molecular and neuronal activity) remodeling in the LHb.

To examine whether this onset may represent a window for effective treatment initiation, we assessed whether limiting LHb neuronal activity at this early stage of CORT-induced remodeling is sufficient to act as antidepressant. Bilateral expression of the inhibitory designer receptor exclusively-activated by designer drugs (G_i-DREADD; Fig. 4d) in the LHb was used in conjunction with the designer drug clozapine *N*-oxide (CNO, i.p., 1 mg kg^{-1}) after 7 days of CORT administration and prior to each behavioral paradigm. In CORT-treated mice expressing a control viral vector (AAV-tdTomato) in the LHb, CNO had no effect, recapitulating the depressive phenotype at *t*7 as indicated by their shifted behavioral state from vehicle-administered mice (Fig. 4e). Instead, reducing LHb neuronal activity via CNO injection in Gi-DREADD mice led to a shift in the behavioral state towards vehicle-treated mice, reducing the clustering accuracy between groups (Fig. 4e, f; Extended Data Fig. 5i). This indicates that limiting LHb neuronal activity at the onset of the behavioral deficits can already normalize depression-related behavioral phenotypes. To establish whether this represents a strategy relevant for therapeutic interventions, we employed ketamine as it efficiently rescues stress-induced neural circuit adaptations (Fig. 3) and fully-manifested depression-related states across

fish, rodents and humans[2,5,31,33,43,54]. The behavioral state was computed at *t*7 of CORT exposure after administration of saline or ketamine (Fig. 4d). Similarly to Gi-DREADD, ketamine treatment was antidepressant as behavioral states were comparable to vehicle-administered mice (Fig. 4e, f; Extended Data Fig. 5f). Together, these data uncovered an early critical period associated with stress susceptibility during which antidepressant actions are effective in rescuing depression-related states.

Discussion

Using longitudinal analysis of the LHb transcriptional landscape, single neuron activity, and behavior, we demonstrate that depression-related phenotypes are spatially and temporally encoded in the LHb during chronic CORT (as a proxy of stress accumulation). To our knowledge, no previous example of spatiotemporal convergence across biological modalities exists within mood disorders research frameworks.

Single-cell transcriptomic analyses of the mammalian habenula uncovered transcriptional diversity, revealing a comprehensive molecular atlas indicative of the function and connectivity of LHb cell types across mice and fish[23,36,39]. In this study, we establish a spatially-resolved chart that recapitulates molecular features of single cells. Interrogation of this atlas reveals that much of the molecular code in the LHb is organized along a medial-to-lateral territorial axis. These molecular domains present functional relevance as they coincide with distinct input-output specializations in the LHb[26,37,44,55], supporting a model of molecularly driven circuit assembly[38].

Transcriptionally distinct LHb cell types are preferentially activated (as indexed by immediate early gene expression) following exposure to aversive experiences[23]. Is this molecular code within LHb cells plastic? The expression of genes encoding for ion channels and synaptic mediators, including *Slc24a2* and *Map1b,* changes in the LHb after an acute stress experience and in susceptible mice displaying depression-related behaviors after chronic mild stress[21,23]. These genetic signatures also changed in our spatial transcriptomic atlas, supporting relationships between molecular adaptations and stress susceptibility across rodent models of depression that extend to precise LHb territories and likely projection targets. The dataset presented here provides a rich resource for identifying biologically meaningful transcriptional alterations across LHb domains, potentially encompassing neuronal, glial, and other cell types in response to stress accumulation. Although the neuronal component of the LHb is critical for

283 the expression of depression-like phenotypes, aberrant function of non-neuronal cells partly
284 contribute to these states[25,56-58]. Future investigations are required to determine the contribution
285 of other cell-types and to which discrete brain circuits the spatially-resolved molecular
286 remodeling pertains to.
287
288 This spatially-resolved transcriptional re-arrangement parallels LHb-distributed adaptations in
289 neuronal activity that emerge over prolonged CORT elevation. A territorial gradient of stress-
290 mediated increased activity within the LHb not only correlates with the molecular adaptations
291 but foremost highlights the relevance of spatially-organized neuronal ensembles instrumental
292 in driving depression-like behaviors[4,29]. In addition to depressive-related states including
293 reduced active coping and emergence of an apathy-like phenotype, our findings support deficits
294 in the encoding of aversive stimuli (i.e. reduction in threat and airpuff-driven escapes)[10]. Thus,
295 a shared onset of a plethora of LHb-dependent depression-related behavioral phenotypes
296 emerge during chronic CORT. Furthermore, a progressive and spatially-biased recruitment of
297 aversion-driven excitation in individual neurons of the zebrafish LHb homologue, ventral
298 habenula, was predictive of the behavioral repercussions of stress[59], supporting shared stress-
299 driven LHb adaptations across species. Although the mechanisms underlying the increased
300 excitation across the lateral territory of LHb were not directly investigated, it is plausible that
301 potentiated synaptic excitation[8,21], reduced inhibitory neurotransmission[7,27], and excessive
302 burst firing patterns[29,30] are fundamental contributors. Our finding that antidepressant-sensitive
303 increased activity of precise neuronal ensembles marks an onset of stress susceptibility is
304 consistent with the above outlined possibilities, although future analysis merging the molecular
305 and functional signatures of specific cell clusters may reveal additional features of altered LHb
306 function[23,43].
307
308 While aberrant LHb neurotransmission and activity is known to contribute to behavioral
309 changes in chronic stress and depression[6,9,37], this work suggests that a critical period for the
310 emergence of stress-induced behavioral phenotypes exists (across different murine stress
311 models; CORT and restraint stress), and it is orchestrated by LHb neuronal activity and
312 molecular remodeling. By demonstrating that a temporally-tailored reduction in LHb activity
313 during stress accumulation —achieved through local chemogenetic manipulations or systemic
314 ketamine administration[33,34]— normalizes neuronal dynamics and behavioral phenotypes
315 associated with susceptibility, our findings suggest targeting the timing of treatment initiation

for therapy refinement. Thus, interventions initiated during early stages of mood disorders may be particularly effective in sustaining the benefits of antidepressants to facilitate remission.

References

1. Krishnan, V. & Nestler, E. J. The molecular neurobiology of depression. *Nature* **455**, 894–902 (2008).
2. Moda-Sava, R. N. *et al.* Sustained rescue of prefrontal circuit dysfunction by antidepressant-induced spine formation. *Science* **364**, eaat8078 (2019).
3. Van Praag, H. M., de Kloet, E. R. & Van Os, J. *Stress, the brain and depression* (Cambridge University Press, 2004).
4. Zheng, Z. *et al.* Hypothalamus-habenula potentiation encodes chronic stress experience and drives depression onset. *Neuron* **110**, 1400–1415.e6 (2022).
5. Cui, Y. *et al.* Astroglial Kir4.1 in the lateral habenula drives neuronal bursts in depression. *Nature* **554**, 323–327 (2018).
6. Hu, H., Cui, Y. & Yang, Y. Circuits and functions of the lateral habenula in health and in disease. *Nat Rev Neurosci* **21**, 277–295 (2020).
7. Lecca, S. *et al.* Rescue of GABAB and GIRK function in the lateral habenula by protein phosphatase 2A inhibition ameliorates depression-like phenotypes in mice. *Nat Med* **22**, 254–261 (2016).
8. Li, B. *et al.* Synaptic potentiation onto habenula neurons in the learned helplessness model of depression. *Nature* **470**, 535–539 (2011).
9. Proulx, C. D., Hikosaka, O. & Malinow, R. Reward processing by the lateral habenula in normal and depressive behaviors. *Nat Neurosci* **17**, 1146–1152 (2014).
10. Shabel, S. J., Wang, C., Monk, B., Aronson, S. & Malinow, R. Stress transforms lateral habenula reward responses into punishment signals. *Proc Natl Acad Sci U S A* **116**, 12488–12493 (2019).
11. Maniatis, S. *et al.* Spatiotemporal dynamics of molecular pathology in amyotrophic lateral sclerosis. *Science* **364**, 89–93 (2019).
12. Ståhl, P. L. *et al.* Visualization and analysis of gene expression in tissue sections by spatial transcriptomics. *Science* **353**, 78–82 (2016).
13. Cameron, L. P. *et al.* A non-hallucinogenic psychedelic analogue with therapeutic potential. *Nature* **589**, 474–479 (2021).
14. Castrén, E. & Monteggia, L. M. Brain-Derived Neurotrophic Factor Signaling in Depression and Antidepressant Action. *Biol Psychiatry* **90**, 128–136 (2021).
15. Duman, R. S., Heninger, G. R. & Nestler, E. J. A molecular and cellular theory of depression. *Arch Gen Psychiatry* **54**, 597–606 (1997).
16. Jauhar, S. *et al.* A leaky umbrella has little value: evidence clearly indicates the serotonin system is implicated in depression. *Mol Psychiatry* **28**, 3149–3152 (2023).
17. Kalisch, R. *et al.* The resilience framework as a strategy to combat stress-related disorders. *Nat Hum Behav* **1**, 784–790 (2017).
18. Sheline, Y. I., Liston, C. & McEwen, B. S. Parsing the Hippocampus in Depression: Chronic Stress, Hippocampal Volume, and Major Depressive Disorder. *Biol Psychiatry* **85**, 436–438 (2019).
19. Tafet, G. E. & Nemeroff, C. B. The Links Between Stress and Depression: Psychoneuroendocrinological, Genetic, and Environmental Interactions. *J Neuropsychiatry Clin Neurosci* **28**, 77–88 (2016).
20. Nestler, E. J. & Russo, S. J. Neurobiological basis of stress resilience. *Neuron* **112**, 1911–1929 (2024).

21. Cerniauskas, I. *et al.* Chronic Stress Induces Activity, Synaptic, and Transcriptional Remodeling of the Lateral Habenula Associated with Deficits in Motivated Behaviors. *Neuron* **104**, 899–915.e8 (2019).
22. Congiu, M. *et al.* Plasticity of neuronal dynamics in the lateral habenula for cue-punishment associative learning. *Mol Psychiatry* **28**, 5118–5127 (2023).
23. Hashikawa, Y. *et al.* Transcriptional and Spatial Resolution of Cell Types in the Mammalian Habenula. *Neuron* **106**, 743–758.e5 (2020).
24. Lecca, S. *et al.* Aversive stimuli drive hypothalamus-to-habenula excitation to promote escape behavior. *Elife* **6**, e30697 (2017).
25. Michel, L. *et al.* Calcium dynamics in habenular astrocytes regulate active coping within behavioral transitions. *Commun Biol* **8**, 1087 (2025).
26. Nuno-Perez, A. *et al.* Stress undermines reward-guided cognitive performance through synaptic depression in the lateral habenula. *Neuron* **109**, 947–956.e5 (2021).
27. Shabel, S. J., Proulx, C. D., Piriz, J. & Malinow, R. Mood regulation. GABA/glutamate co-release controls habenula output and is modified by antidepressant treatment. *Science* **345**, 1494–1498 (2014).
28. Yang, L. *et al.* Stress dynamically modulates neuronal autophagy to gate depression onset. *Nature* **641**, 427–437 (2025).
29. Yang, Y. *et al.* Ketamine blocks bursting in the lateral habenula to rapidly relieve depression. *Nature* **554**, 317–322 (2018).
30. Zhukovskaya, A. *et al.* Heightened lateral habenula activity during stress produces brainwide and behavioral substrates of susceptibility. *Neuron* **112**, 3940–3956.e10 (2024).
31. Chen, M. *et al.* Brain region-specific action of ketamine as a rapid antidepressant. *Science* **385**, eado7010 (2024).
32. Li, G. *et al.* Instantaneous antidepressant effect of lateral habenula deep brain stimulation in rats studied with functional MRI. *Elife* **12**, e84693 (2023).
33. Ma, S. *et al.* Sustained antidepressant effect of ketamine through NMDAR trapping in the LHb. *Nature* **622**, 802–809 (2023).
34. Tchenio, A., Lecca, S., Valentinova, K. & Mameli, M. Limiting habenular hyperactivity ameliorates maternal separation-driven depressive-like symptoms. *Nat Commun* **8**, 1135 (2017).
35. Lalive, A. L. *et al.* Synaptic inhibition in the lateral habenula shapes reward anticipation. *Curr Biol* **32**, 1829–1836.e4 (2022).
36. Lecca, S. *et al.* A neural substrate for negative affect dictates female parental behavior. *Neuron* **111**, 1094–1103.e8 (2023).
37. Michel, L., Molina, P. & Mameli, M. The behavioral relevance of a modular organization in the lateral habenula. *Neuron* **112**, 2669–2685 (2024).
38. Schmidt, E. R. E. *et al.* Subdomain-mediated axon-axon signaling and chemoattraction cooperate to regulate afferent innervation of the lateral habenula. *Neuron* **83**, 372–387 (2014).
39. Wallace, M. L. *et al.* Anatomical and single-cell transcriptional profiling of the murine habenular complex. *Elife* **9**, e51271 (2020).
40. Fetcho, R. N. *et al.* A stress-sensitive frontostriatal circuit supporting effortful reward-seeking behavior. *Neuron* **112**, 473–487.e4 (2024).
41. Gourley, S. L. & Taylor, J. R. Recapitulation and reversal of a persistent depression-like syndrome in rodents. *Curr Protoc Neurosci* **Chapter 9**, Unit 9.32 (2009).
42. Karatsoreos, I. N. *et al.* Endocrine and physiological changes in response to chronic corticosterone: a potential model of the metabolic syndrome in mouse. *Endocrinology* **151**, 2117–2127 (2010).

43. Sylwestrak, E. L. *et al.* Cell-type-specific population dynamics of diverse reward computations. *Cell* **185**, 3568–3587.e27 (2022).
44. Shabel, S. J., Proulx, C. D., Trias, A., Murphy, R. T. & Malinow, R. Input to the lateral habenula from the basal ganglia is excitatory, aversive, and suppressed by serotonin. *Neuron* **74**, 475–481 (2012).
45. Han, L. *et al.* Single-cell spatial transcriptomic atlas of the whole mouse brain. *Neuron* **113**, 2141–2160.e9 (2025).
46. Goes, F. S. *et al.* Large-scale transcriptomic analyses of major depressive disorder reveal convergent dysregulation of synaptic pathways in excitatory neurons. *Nat Commun* **16**, 3981 (2025).
47. Wu, J. *et al.* Integrating spatial and single-nucleus transcriptomic data elucidates microglial-specific responses in female cynomolgus macaques with depressive-like behaviors. *Nat Neurosci* **26**, 1352–1364 (2023).
48. Dieterich, A. *et al.* Chronic corticosterone administration induces negative valence and impairs positive valence behaviors in mice. *Transl Psychiatry* **9**, 337 (2019).
49. Miranda, M. I., Quirarte, G. L., Rodriguez-Garcia, G., McGaugh, J. L. & Roozendaal, B. Glucocorticoids enhance taste aversion memory via actions in the insular cortex and basolateral amygdala. *Learn Mem* **15**, 468–476 (2008).
50. Wang, D. *et al.* Learning shapes the aversion and reward responses of lateral habenula neurons. *Elife* **6**, e23045 (2017).
51. Casarotto, P. C. *et al.* Antidepressant drugs act by directly binding to TRKB neurotrophin receptors. *Cell* **184**, 1299–1313.e19 (2021).
52. Kasper, S. Is treatment-resistant depression really resistant? *Eur Neuropsychopharmacol* **58**, 44–46 (2022).
53. von Ziegler, L. M. *et al.* Analysis of behavioral flow resolves latent phenotypes. *Nat Methods* **21**, 2376–2387 (2024).
54. Berman, R. M. *et al.* Antidepressant effects of ketamine in depressed patients. *Biol Psychiatry* **47**, 351–354 (2000).
55. Stamatakis, A. M. *et al.* A unique population of ventral tegmental area neurons inhibits the lateral habenula to promote reward. *Neuron* **80**, 1039–1053 (2013).
56. Aizawa, H. *et al.* Potassium Release From the Habenular Astrocytes Induces Depressive-Like Behaviors in Mice. *Glia* **73**, 759–772 (2025).
57. Valentinova, K. *et al.* Morphine withdrawal recruits lateral habenula cytokine signaling to reduce synaptic excitation and sociability. *Nat Neurosci* **22**, 1053–1056 (2019).
58. Xin, Q. *et al.* Neuron-astrocyte coupling in lateral habenula mediates depressive-like behaviors. *Cell* **188**, 3291–3309.e24 (2025).
59. Andalman, A. S. *et al.* Neuronal Dynamics Regulating Brain and Behavioral State Transitions. *Cell* **177**, 970–985.e20 (2019).

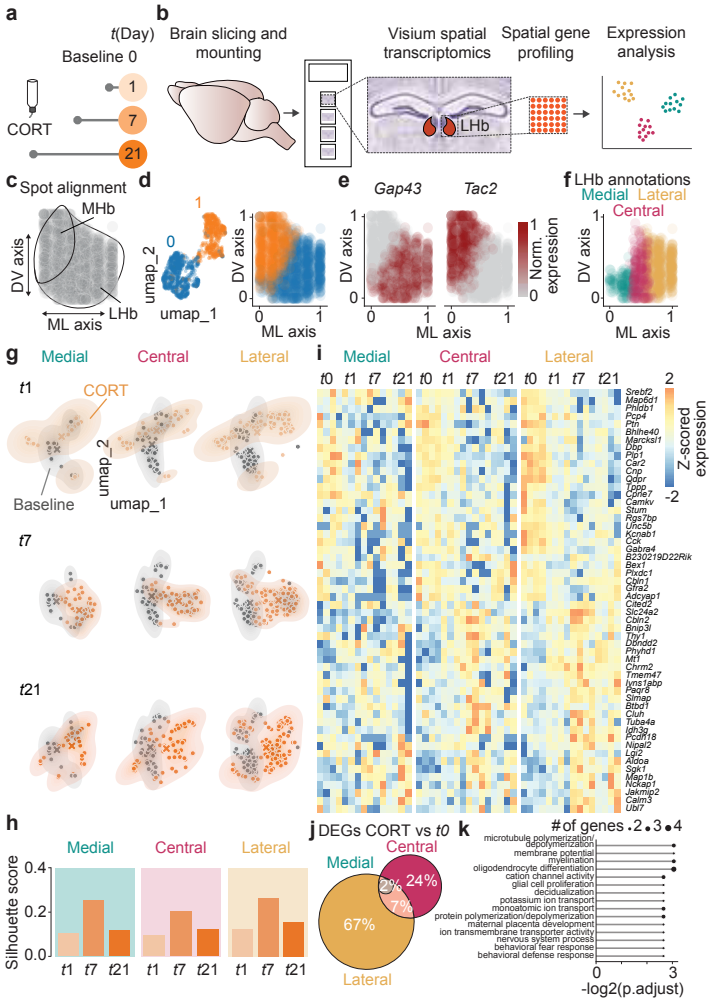

Molina et al., Figure 1

Figure 1. Remodeling of a LHb molecular cartography in depression. **a,** Schematic of the experimental design. **b,** Schematic of the experimental protocol. **c,** Alignment of all spots from the habenular complex (Hb; LHb, lateral habenula; MHb, medial habenula) into a common coordinate framework (ML, medio-lateral; DV, dorso-ventral) within the Hb anatomical structure. **d,** Uniform Manifold Approximation and Projection (UMAP) visualization of the unsupervised clustering of Hb spots and their distribution within the coordinate frame color coded by cluster identity. **e,** Distribution of the spots within the common coordinate framework colored according to normalized expression of canonical LHb and MHb markers (*Gap43* and *Tac2*, respectively). **f,** Annotation of LHb subterritories into medial, central and lateral. **g, h,** Top, UMAP visualization of LHb spots at baseline versus after 1, 7 or 21 days of CORT treatment across LHb subterritories. Crosses represent group centroids. Bottom, corresponding pairwise silhouette scores calculated in the low-dimensional embeddings (PCA). **i,** Heatmap showing the scaled expression levels of differentially expressed genes (DEGs) throughout CORT treatment and subterritories. **j,** Venn diagram showing overlap of DEGs across CORT treatment compared to baseline between each LHb subterritory. **k,** Top 15 Gene Ontology enrichment analysis terms (biological process) of the DEGs in the lateral LHb.

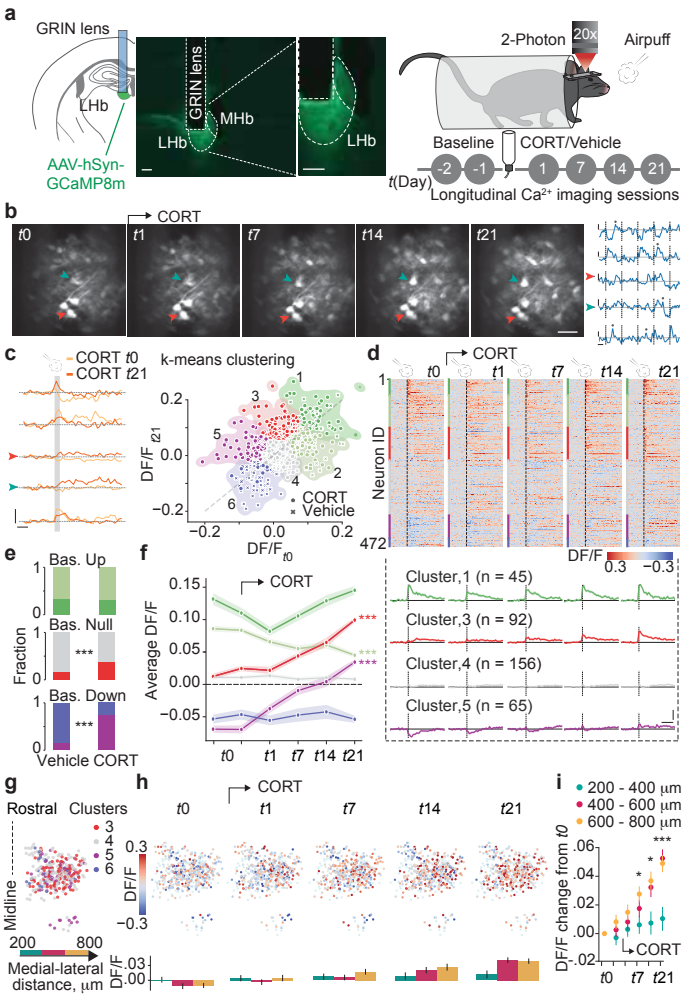

Molina et al., Figure 2

Figure 2. Spatiotemporal dynamics of LHb neuronal activity across chronic CORT. a, Schematic of AAV-hSyn-GCaMP8m injection and GRIN lens implant in LHb with histological verification (scale bars, 200 μm). Right, experimental settings and timeline for longitudinal two-photon recordings. **b,** Average projection from representative FOV from one mouse imaged across baseline (*t0*), and days 1, 7, 14, and 21 of CORT treatment (scale bar, 100 μm). Arrowheads indicate neurons tracked across all sessions. Right, calcium traces from a subset of neurons from example FOV at baseline 1 indicating ongoing and time-locked activity. Dots indicate spontaneous transients, and dashed lines represent airpuffs (scale bars, 0.2 DF/F, 5 s). **c,** Trial-average airpuff responses of neurons in (b) at *t0* and *t21* (scale bars, 0.2 DF/F, 1 s) and population DF/F responses in vehicle- and CORT-treated mice at *t0* vs *t21*. Neurons color-coded by cluster identity; shadow represent kernel density estimation for each cluster. **d,** Heatmaps of trial-averaged airpuff responses (dashed line) of individual neurons across sessions (n = 472 cells, 17 mice) sorted by cluster identity. Bottom, cluster-averaged airpuff responses across sessions (scale bars, 0,1 DF/F, 1 s). **e,** Proportion of neurons per cluster within each category (increased, unchanged, or reduced airpuff response at baseline) in vehicle- vs CORT-treated mice (Chi-square contingency test, X2 = 0, $P = 1$; X2 = 7.88, $^{**}P = 0.005$; X2 = 50.02, $^{***}P < 0.001$, respectively). **f,** Averaged cluster responses to airpuff across sessions in CORT mice (two-way repeated measures (RM) ANOVA followed by Benjamini/Hochberg FDR correction (Interaction, $F_{25,2330} = 25.66$, $P < 0.001$). **g,** Spatial projection onto the horizontal plane of clusters 3-6 in CORT mice. **h,** Spatial projection of all neurons in CORT mice with superimposed color-coded airpuff response of clusters 3-6 across sessions. Below, average airpuff responses per 200 μm medio-lateral bin. **i**, Average airpuff-driven DF/F change from *t0* across bins and sessions (two-way RM ANOVA, followed by Benjamin/Hochberg FDR correction, Interaction, $F_{10,1660} = 3.52$, $P < 0.001$). Data represented as mean ± s.e.m. * $P < 0.05$, $^{**}P < 0.01$, $^{***}P < 0.001$.

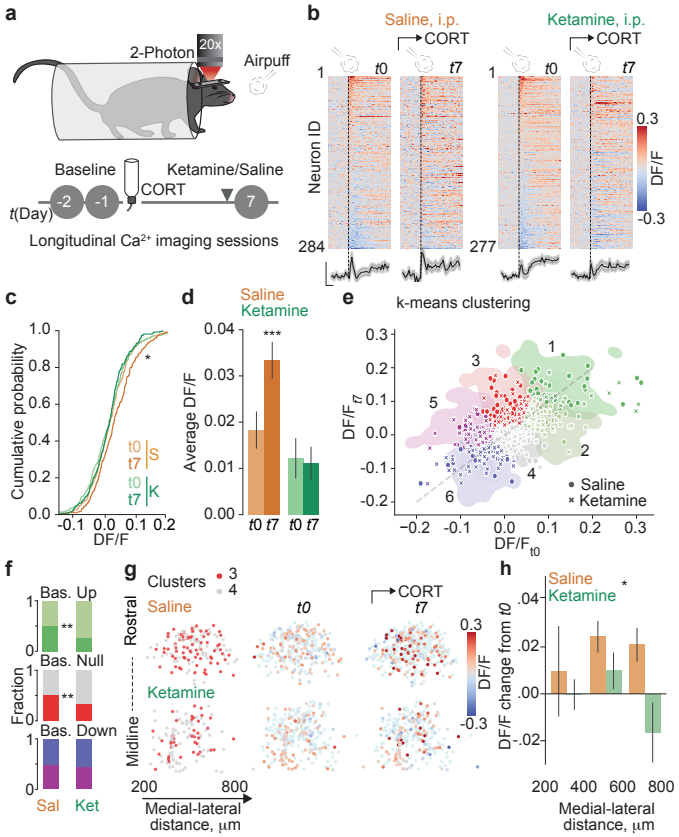

Molina et al., Figure 3

Figure 3. Antidepressant-purposed ketamine restores CORT-mediated LHb remodeling. **a,** Schematic of experimental settings and timeline for two-photon recordings. **b,** Heatmaps trial-average of airpuff responses (dashed line) of individual neurons at *t0* (average baseline 1 and 2 sessions) and day 7 of CORT treatment in mice administered with saline (n = 284 cells, 8 mice) or ketamine (10 mg kg^{-1}; n = 277 cells, 8 mice). Bottom, average population traces for each group (scale bars, 0,05 DF/F, 1 s). **c,** Distribution of DF/F responses to airpuff at *t0* and day 7 CORT in saline- (S) and ketamine- (K) treated mice (Kolmogorov-Smirnov test, $P = 0.46$ and $P < 0.001$ at *t0* and *t7* CORT, respectively). **d,** Average response magnitude at *t0* and *t7* CORT in saline- and ketamine-treated mice (Two-way RM ANOVA followed by Bonferroni correction, Interaction, $F_{1,559} = 9.9$, $P = 0.002$). **e,** Average airpuff responses from all neurons in saline- (circle) and ketamine-treated (crosses) groups at t0 (average of baseline 1 and 2) vs day 7. Neurons color-coded by cluster identity; shadow represents kernel density estimation of the original clusters (see Methods). **f,** Proportion of neurons per cluster within each category (increased, unchanged, or reduced airpuff response at baseline) in saline- vs ketamine-treated mice (Chi-square contingency test, X2 = 7.254, $^{**}P = 0.007$; X2 = 7.210, $^{**}P = 0.007$; X2 = 0.135, $P = 0.71$, respectively). **g,** Left, spatial projection onto the horizontal plane of clusters 3 and 4 in saline- (top) and ketamine-treated mice (bottom). Middle and right, spatial projection onto horizontal plane of all recorded neurons with superimposed color-coded airpuff response of clusters 3 to 4 at baseline and day 7 in saline- (top) and ketamine-treated mice (bottom). **h,** Average airpuff-induced DF/F change from *t0* across bins at day 7 in saline- and ketamine-treated mice (Two-way ANOVA followed by Benjamin/Hochberg FDR correction, Treatment, $F_{1,253} = 6.28$, $^{*}P = 0.013$). Data represented as mean ± s.e.m.

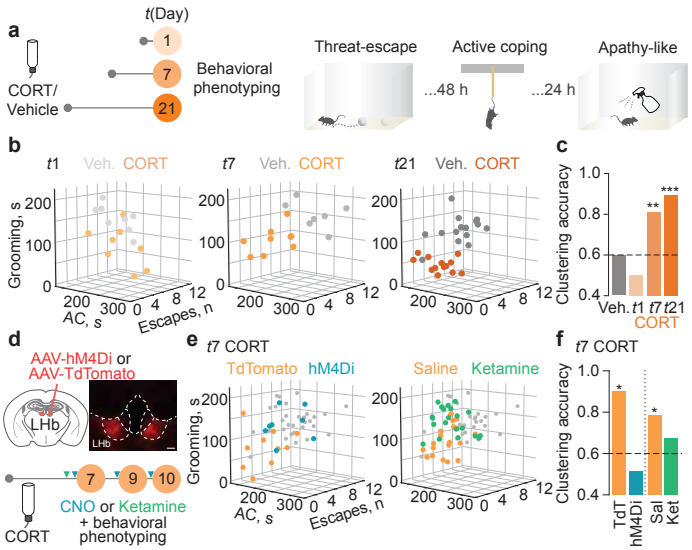

Molina et al., Figure 4

Figure 4. Time-resolved emergence of behavioral signatures of depression. a, Schematic of experimental design. Independent cohorts of mice were treated either with CORT (0.1 mg ml^{-1}) or vehicle (1% ethanol) in their drinking water for 1 (n_{Veh} = 8, n_{CORT} = 8), 7 (n_{Veh} = 8, n_{CORT} = 8), or 21 days (n_{Veh} = 15, n_{CORT} = 13), and exposed to a battery of behavioral tests (threat-escape, tail suspension test, apathy-like behavior). **b,** 3-dimensional plots showing individual behavioral scores –threat-evoked anticipatory escapes, active coping (AC, s) in the tail suspension test and grooming time in the apathy scoring – from vehicle- and CORT-treated mice after 1 (left), 7 (middle) or 21 (right) days of treatment. **c,** Clustering accuracy from k-means classification using standardized behavioral scores. Average accuracy of classifying one vehicle (Veh) group versus remaining Veh groups (grey), and classification accuracy of CORT-treated mice versus their respective time-matched Veh group (orange). Significance determined by bootstrap (**$P < 0.01$,***$P < 0.001$, see Methods). **d,** Schematic of bilateral AAV-hM4Di-mCherry injection in the LHb with representative histological verification (Scale bar, 200 μm). Below, experimental timeline for CORT treatment, behavioral phenotyping and i.p. administration of CNO (1 mg kg^{-1}). **e,** Left, 3-dimensional plot showing behavioral scores (as in b) for individual mice treated with CORT for 7 days and injected either with control virus (TdTomato-CORT, n = 10) or with Gi-DREADD (hM4Di-CORT, n = 8). Right, 3-dimensional plot showing behavioral scores for individual mice treated with CORT for 7 days and injected either with saline (n = 20), or ketamine (n = 21). Grey data points in both plots represent the distribution of all vehicle-treated mice from (b) for comparison. **f,** Clustering accuracy from k-means classification comparing TdTomato-CORT (TdT), hM4Di-CORT (hM4Di), Saline-CORT (Sal) or Ketamine-CORT (Ket) versus all Vehicle-treated mice. Statistical significance assessed by bootstrap.

Methods

Experimental subjects

C57BL/6J wild-type male mice (8-20 weeks old; Janvier Labs, France) were used in this study. Mice were housed in groups of 3-4 per cage in individually ventilated cages enriched with nesting material and tunnels (IVC, Innovive, France) with ad libitum access to water and food on a 12:12 h light:dark cycle (lights on at 07:00). Mice were randomly assigned to experimental group at their arrival in the animal facility. All experimental procedures were conducted in accordance with the Swiss National Institutional Guidelines on animal experimentation and were approved by the canton of Vaud Cantonal Veterinary Office Committee for Animal Experimentation (Switzerland; License VD3798).

Corticosterone administration

Drinking water was replaced with a solution containing corticosterone (CORT, Sigma-Aldrich, Cat# 27840). CORT was dissolved in 100% ethanol and then diluted in water to a final CORT concentration of 0.1 mg/ml and ethanol concentration of 1%. Fresh CORT solutions were replaced every 72 hours to minimize CORT degradation. Control mice received 1% ethanol in water. Chronic administration of CORT, the key mediator of the rodent stress response, is a model capable to produce depression- related behaviors yet it leads in parallel to metabolic alterations[1-3]. Thus, to test whether CORT effects on behavior generalize to other forms of chronic stress, we repeated these experiments in mice exposed to chronic restraint stress. Mice were placed in 50-ml Falcon tubes with holes for air flow for 2–3 h per day for either 1, 7, or 21 days[4].

Drugs

All drugs but CORT were dissolved in 0.9% saline and injected intraperitoneally (i.p.). Concentrations were as follows: Clozapine-N-oxide (Hello Bio, UK, Ref. HB6149) at 1 mg kg^{-1}, and ketamine (mixture of *R*-ketamine and *S*-ketamine; Labatec, Switzerland) at 10 mg kg^{-1}.

Stereotaxic surgeries for viral injections

Mice (8-week-old) were anesthetized with ketamine/xylazine (150/10 mg kg^{-1}, i.p., Cantonal University Hospital, Lausanne, Switzerland) and placed on a stereotaxic frame (Kopf, France). The ocular protector Viscotear® was used to prevent eye damage. After scalp incision, holes were drilled above the LHb at coordinates: AP -1.5 mm, ML ±0.45 mm, DV: -2.8 mm (from

Bregma). The following viral constructs were injected using a glass pipette: AAVDJ-hSyn1-GCaMP8m (unilateral), AAV9-hSyn-hM4Di-IRES-mCherry (bilateral) and AAV9-hSyn-TdTomato (bilateral). All constructs were purchased from the Zurich University Viral Vector Core. Injections were performed at a rate of 100-150 nl/min, and the pipette was withdrawn from the brain 10 minutes post-infusion.

Chronic lens implants

Following a two-week recovery period, mice underwent lens implantation for two-photon calcium imaging. Animals were anesthetized with isoflurane (induction: 3.5–4%, maintenance: 2–2.4%, Univentor) and implanted with a gradient refractive index (GRIN) lens (6.1 mm length, 0.5 mm diameter; Bruker Inscopix, USA). The lens was positioned approximately 150–200 µm above the injection site using the following coordinates relative to Bregma: −1.45 mm AP, 0.45 mm ML, and −2.70 to −2.75 mm DV from the brain surface. The lens was lowered at a constant speed of 1 µm/s. Prior to lens implantation, a pre-tract was made using a 0.5 mm diameter needle at the same coordinates, reaching a depth of –2.5 mm from brain surface. Throughout the surgical procedure, 0.9% saline was continuously applied to the cortical surface to maintain hydration at the entry site. Later, the skull was scraped clean and a stainless steel headbar was implanted above lambda and everything was secured to the skull using Super-Bond™ dental adhesive resin cement (Universal Kit; Sun Medical Co., Japan). A custom 3D-printed PLA head-ring was placed on top of the first cement layer surrounding the GRIN lens to protect it from damage and secured with another layer of cement. For pain management, paracetamol (500 mg/250 ml; 200-300 mg/kg/day) was added to drinking water after the surgery.

Histological processing and microscopy

Mice were terminally anesthetized with pentobarbital and transcardially perfused with 4% paraformaldehyde (PFA) in 0.1 M phosphate-buffered saline (PBS). Brains were collected and post-fixed overnight in 4% PFA at 4 °C. Consecutive coronal slices (60–80 microns) were sectioned using a vibratome (Leica VT1200S). Images were acquired with an epi-fluorescent microscope (Axio imager, Zeiss) to confirm correct targeting of the LHb, and we excluded mice whenever this was not achieved (not targeted viral expression and/or GRIN lens misplacement).

Two-photon recordings

Before the two-photon recordings started, mice were handled for 2 days and habituated to head fixation for at least 4 days. Mice received 20 unpredicted airpuffs (0.5 s duration, 3.75 bar) via a 25-gauge needle directed at the right eye with a variable ITI of 1-2 minutes (Congiu et al., 2023). For ketamine experiments, ketamine was injected i.p. 18h and 3h before two-photon recordings.

Two-photon microscopy experiments were conducted to visualize LHb neuronal calcium dynamics *in vivo* in response to airpuff. Baseline recordings started when the FOV was stable for at least 2-3 weeks. Acquisition was performed with a two-photon Ultima Investigator microscope (Bruker Fluorescence Microscopy, USA) combined with a Chameleon-Ultra Tunable Laser (Coherent) and equipped with an Olympus 20X air objective (LCPLN20XIR). Images were acquired at 30 Hz using a galvo-resonant scanner and a 6 times temporal average was performed online for an effective frame rate of 5 Hz with a resolution of 512 × 512 pixels. At each trial, recordings started 6 s before air puff delivery, and a 15s-long video was collected using Prairie view software (Bruker Fluorescence Microscopy, USA). Prior to the start of experiments, 1-3 FOVs per mouse were chosen to maximize the number neurons recorded by adjusting the imaging plane (z-axis), and each FOV was spaced at least 60 μm apart to prevent visualization of the same cells across multiple FOVs.

Two-photon recordings analysis and data processing

Acquired videos were motion-corrected using CaImAn package. The motion corrected file and average projections across all motion corrected frames were imported into ImageJ (Fiji, v1.54) for selecting regions of interest (ROIs) corresponding to neuronal somas. ROIs were manually drawn by an observer blind to experimental condition using the polygon selection tool only around cells that were reliably tracked across the different imaging sessions. The same ROI was used across sessions with minimal adjustments based on potential small shifts of the FOV between sessions. Next, calcium transient time series data were extracted with the ImageJ BAR plug-in and analyzed using custom Python scripts. DF/F was calculated on a trial-by-trial basis as: (F-F0)/F0, F0 being the 3s preceding the airpuff. Response to the airpuff was defined as the area under the curve (AUC) of DF/F during 1s following airpuff onset.

To classify neurons as excited, non-responding, or inhibited by airpuff during a single recording session, a two-sample Wilcoxon rank-sum test was used to assess whether airpuff response was significantly different from DF/F AUC 1.5s prior to airpuff onset (significance threshold of $p \leq 0.05$). To identify distinct response phenotypes across the experimental

timeline, airpuff responses were trial-averaged, with baseline1 and baseline2 sessions being merged into a single baseline. K-means clustering was simultaneously performed on neurons recorded from both CORT and vehicle mice, using airpuff responses at baseline and D21 sessions as independent variables. Number of clusters was initially chosen in the range 3-8 as suggested by the elbow method, and finally set at 6, which provided the best interpretability of response phenotypes. Neurons recorded in the ketamine treatment experiment were embedded into the same 6 clusters using one-step k-means clustering with pre-initialized centroids. Centroids were defined using per-cluster average airpuff responses at Baseline and *t7* CORT session of the original dataset (see Fig. 2).

To reconstruct the location of the recorded neurons within the LHb horizontal plane, we first determined overall GRIN lens placement by aligning post-hoc fixed brain sections to the stereotactic Paxinos atlas of the mouse brain. We identified the center-point and the edges of the bottom of the lens to register each recorded FOV onto a horizontal plane. The final position of the recorded neurons on the LHb map was defined as a sum of their coordinates within the FOV and the coordinates of the respective GRIN lens within the brain.

Behavioral paradigms

Mice were housed in the facility for at least 6 days prior to any experiment and handled for 2-3 days before experiments. Behavioral evaluation was conducted under low light conditions (15 to 25 lux) at a controlled temperature (21-22 °C). On test days, mice were habituated to the behavioral room for at least 20-30 min. All behavioral experiments were videotaped for offline analysis. Behavioral experiments in for DREADDi experiments were performed 4 weeks after injection, and Clozapine-N-Oxide (CNO) was administered 20-30 min prior testing. For ketamine experiments, ketamine was injected i.p. 18h and 3h prior to behavioral assessment.

Airpuff-driven escape

The paradigm was conducted in a custom-made plastic transparent chamber (9(w)x34(l)x12.7(h)cm) fitted with two 3D-printed manifolds 7 cm-wide containing three 1 mm-diameter holes. The manifolds were attached to the two opposite short walls at 2.5 cm from the floor of the cage. The cabling system was connected on one extreme to the manifold and on the other to an air compressor to deliver airpuffs (4.75 bars). Mice were allowed to explore the cage for 3 min and then 10 airpuffs were delivered with an inter-trial interval (ITI) of 1-2 minutes whenever the mouse entered an area within 4 cm in front of the manifold.

Airpuff delivery had a maximal duration set to 3 s and was terminated when the mouse exited the 4cm-wide area (computed as escape).

Open field

Mice were placed in an arena (45(w)x45(l)x40(h)cm) for 5 min and video recording was controlled with EthovisionXT 15 (Noldus Information Technology, The Netherlands). Mice were tracked using EthovisionXT to extract the distance traveled and time spent in the center (30 x 30 cm).

Threat challenge

We designed a task to measure innate defensive responses to an approaching operator-controlled threat. Mice were placed in an open field (OF) where a robotic ball (Sphero mini®) remotely controlled by the experimenter was directed toward them for 15 trials during 5 min. Video recording was controlled with EthovisionXT 15. Anticipatory escape responses (i.e., movements away from the path of the ball prior to potential contact) were scored manually by blinded observers. Mice were also exposed to the robotic ball stationary placed in the center of the OF before and after testing to measure the time interacting with the ball (automatically tracked with EthovisionXT, noise-point body tracking within a 4-cm distance range of the ball).

Tail suspension

Mice were suspended by fixing its tail with adhesive tape, 50 cm above the surface for 6 min. A plastic tube was placed around the base of the tail to prevent tail climbing behavior. Both immobility and active coping time were scored by an observer blind to experimental conditions.

Apathy-like phenotype

Mice were placed in a Phenotyper box (Noldus, 58(h)x30(l)x30(w)cm) with standard wood chip bedding. After 5 min habituation, a 10% sucrose solution was sprayed on the dorsal coat of the mouse and the time spent grooming was scored for 5 min as an index of self-care behavior (Yalcin et al., 2005).

Behavioral analysis

To characterize CORT or CRS-induced shift in behavioral phenotype, the number of anticipatory escapes during threat challenge, time spent struggling in the TST and grooming time during the apathy-like paradigm were standardized within a subset of experimental groups at a time. We then performed k-means clustering with k=2 clusters and computed accuracy of

assigned clusters to quantify the degree of separation between one of these groups versus the rest in the subset. Bootstrap method was used to statistically test whether the clustering accuracy computed between experimental and control groups was significantly higher than the one computed between controls. In brief, a new dataset was randomly drawn from the original subset of groups by using sampling with replacement and clustering accuracy was calculated. This process was repeated 1000 times, providing a distribution of outcomes. Proportion of outcomes with clustering accuracy below 60% (average of intra-control accuracy) was taken as a significance p-value.

Spatial transcriptomics

Tissue preparation

Mice were deeply anesthetized with pentobarbital and rapidly perfused with 0.1 M phosphate buffered saline (PBS) followed by 4% paraformaldehyde (PFA) in PBS. Brains were removed, post-fixed for 24 h in 4% PFA and cryoprotected in 30% sucrose in PBS at 4 °C. Brains were trimmed into blocks containing the LHb and embedded in Tissue-Tek O.C.T., snap frozen using isopentane and dry ice, and stored at -80 °C. Coronal sections were cryosectioned at 10 µm at -20 ° (Leica CM3050S) and immediately placed on pre-chilled SuperFrost™ slides. Following a rehydration step, sections were stained with a combination of hematoxylin (MHS16, Sigma) and eosin (HT110116, Sigma) solutions in accordance with the Visium CytAssist Rehydration, H&E Staining, Imaging & Decrosslinking protocol (10X Genomics). Coverslips were mounted in 85% glycerol in water medium prior to image acquisition on a Zeiss Axioscan Z.1 equipped with a Plan Apochromat 10x/0.45 objective and a 3CCD Hitachi HV-F202SCL camera. Following coverslip removal, slides were placed on cassettes and the destaining was performed with the addition of 0.1N HCl at 42°C for 15 min followed by the decrosslinking step. Sections were then processed according to the Visium CytAssist Spatial Gene Expression protocol (10X Genomics).

Briefly, sections were incubated in a probe hybridization solution (containing between ~1 and ~3 specific probe per targeted gene) overnight at 50°C. Pairs of probes were then ligated to only bridge the probe pairs that have been hybridized to RNA. After an Eosin staining, sections were placed into the Visium CytAssist instrument to perform the RNA digestion. Ligation were transferred and captured on the spot-barcoded Visium slide. Unique molecular identifiers (UMI) were then added to the ligation ensuring unique spatially-barcoded ligation products. Probes were finally eluted from the slide before the pre-amplification step that generated ample material for the library construction.

cDNA library preparation and sequencing

Spatial transcriptomics libraries were prepared according to the Visium Spatial Gene Expression User Guide: after a SPRIselect (Beckman Coulter) cleanup pre-amplification material was collected for qPCR (CFX OPUS 96, Bio-Rad) determination of sample index PCR cycle number for gene expression libraries preparation. Finally, pre-amplified material underwent indexing with sample indexing PCR based on qPCR Cq values determination to generate final library molecules, before a final SPRIselect cleanup and an assessment of DNA concentration with a Qubit instrument (Thermo Fisher). Sequencing was performed on an AVITI (Element Biosciences) at a sequencing depth of 129±10 million reads per sample.

Raw FASTQ files and paired H&E histology images were processed with Space Ranger software (version 3.1.3, 10x Genomics) using the mm10-2020-A transcriptome reference for alignment and gene counting.

Downstream quality control and analysis were performed in Seurat (v5.1.0)[5]. For each spot, we computed quality control metrics, including the number of detected genes and the number of unique molecular identifiers (UMIs). Spots with fewer than 3,000 UMIs or fewer than 1,500 detected genes were excluded. In addition, mitochondrial genes and unannotated transcripts (i.e., *Gm* and *Rik* genes) were removed from subsequent analyses.

Spots belonging to the habenula (Hb) were identified in Loupe Browser (v8.1.2) by reference to the Allen Mouse Brain Atlas. The lateral habenula (LHb) was further subdivided into medial, central, and lateral domains (mLHb, midLHb, lLHb). Regions corresponding to tissue folds or damaged areas were manually excluded using the drawing tool in Loupe Browser.

Overall, we analyzed 32 coronal sections containing the habenula (n = 4 per cohort, with 2 technical replicates each). Each section yielded a median of 50 spatially barcoded spots per habenular complex, with a median sequencing depth of 7,664 UMIs and 3,844 detected genes per spot.

To embed all Hb spots into a common coordinate framework, custom python scripts were used to apply linear transformations (translation, rotation, and mirroring) to each slice until the habenula, midline, and hippocampal landmarks were aligned. Finally, coordinates of Hb spots from individual slices were scaled to fit a normalized 1x1 bounding box. A custom Python script was used to produce spatial expression gradients. In brief, standardized x and y

coordinates of all Hb spots were binned into 100x100 bins, and normalized expression values from these spots were accumulated per each x-y coordinate into a 100x100 null matrix, creating a 100x100 pixel image. This image was further confined within the manually drawn anatomical LHb mask, and gaussian blur with a 1x1 kernel was applied to smoothen out the resulting gradient of expression.

Transcriptomics downstream analysis

Downstream analyses were performed in Seurat (v5.1.0)[5]. Raw counts were normalized and scaled using SCTransform, applied independently to each tissue section to mitigate inter-slide variability and avoid spurious identification of variable genes. Highly variable genes were selected for each section, and the union of variable features across all sections was used for dimensionality reduction. Principal component analysis (PCA) was performed on this combined feature set to capture major sources of variation across spots. To filter LHb spots, we performed unbiased clustering of all Hb spots in the principal component space using FindClusters function from Seurat package (Louvain algorithm). UMAP embeddings were computed for visualization.

Pseudobulk spatio-temporal analysis

To assess spatial and temporal transcriptional dynamics, spot-level counts were aggregated into pseudobulk profiles, defined as the sum of counts across all spots within each habenular subregion and animal. Technical replicates were collapsed at this stage. Pseudobulk count matrices were normalized and tested for differential expression using DESeq2 (v1.42.1)[6]. DEGs were identified using the Likelihood Ratio Test with LHb subregion and time point (baseline, day 1 and day 7) as model covariates (adjusted p-value < 0.05). We then took this list of pseudobulk DEGs and ran this list through EnrichGO (against all tested genes). 'Positive/negative regulation of' GO terms (biological processes) were collapsed under the same umbrella of 'Regulation of'. Cross validation with published datasetsFor the cross validation of our DEG results, we utilized two published transcriptomic datasets[7,8]. Hashikawa et al. dataset was analyzed utilizing code from the open repository of the authors for preprocessing and clustering of single-cell data, namely first two notebooks: "200309 Doublet Detection" and "200309 Seurat Clustering after doublet detection". Clusters were merged until each cell-type was represented by only one cluster, after which Seurat DotPlot visualization was used to investigate expression levels of top 40 spatially biased genes from the present dataset in different cell-types of Hashikawa et al. dataset. To investigate the overlap between

CORT-sensitive genes of the present dataset and aversion-sensitive Hb genes from the Hashikawa et al. dataset, we used the FindMarkers function from the Seurat package to identify DEGs in control vs. footshock-exposed animals of the Hashikawa et al. dataset. We then quantified the proportion of lLHb DEGs of the present dataset which also showed adjusted p-value<0.05 in the Hashikawa et al. dataset (Extended Fig. 2). To analyze Cerniauskas et al. dataset we utilized normalized gene counts data provided by authors. DEGs were identified using Wilcoxon rank-sum test between cells recorded in animals which underwent chronic mild stress and showed depressive phenotype (TST+ in the paper) vs. control animals without depressive phenotype (TST- in the paper). Genes that showed adjusted p-value<0.05 in present dataset and p-value<0.1 in the Cerniauskas dataset were considered as overlapping (Extended Data Fig. 2).

Han et al.[9] single-cell spatial transcriptomics dataset was used to cross-validate genes with spatial expression bias identified in the present study. For this purpose, we utilized scaled and spatially binned RNA expression data in slices containing LHb (markdown file "T311_T319_SCT_merge_bayes_anno.rds" in the data repository provided by authors). Individual slices containing LHb were aligned and scaled so that bins belonging to LHb match the 1x1 bounding box, creating common coordinate framework. We then computed spatial gradients of gene expression in Han et al. dataset for top 20 genes with highest loading on PC1 from the present study.

Statistics and reproducibility

Animals were randomly assigned to experimental groups. Data are represented as mean ± s.e.m. or in box plots, with center lines indicating the median and whiskers representing minimum-to-maximum. Sample sizes were chosen based on published studies and previous experiments in the laboratory. Individual data points are shown when practical. Most experiments were replicated in multiple independent cohorts of animals. Statistical analysis was performed in Prism 9.5.1 (GraphPad, San Diego, CA, USA) and Python using the Scipy package. Automated analysis and manual analysis by blind experimenters were performed whenever possible. The significance threshold was held at $\alpha = 0.05$ and all statistical tests were two-sided. For normally distributed data, unpaired Student's t-test was used for two sample datasets, and ANOVA for more than two comparison groups. Non-parametric tests were used for non-Gaussian distributions when appropriate: Wilcoxon signed-rank test and Mann-Whitney U-test for paired and unpaired testing for two comparison groups, respectively, and Kruskal-Wallis for more than two groups. P values were corrected for multiple comparisons

when needed. Chi-Square contingency test was performed for comparison of categorical distributions between groups. More detailed information about statistical analysis can be found in Extended Data Table 2.

Data availability

The datasets generated and analyzed during the current study are available in the public Zenodo repository, https://doi.org/10.5281/zenodo.17251142.

Code availability

The code used for analysis (Python) is available through the following public repository **Zenodo,** https://doi.org/10.5281/zenodo.17251142.

Methods references.

1. Gourley, S. L. & Taylor, J. R. Recapitulation and reversal of a persistent depression-like syndrome in rodents. *Curr Protoc Neurosci* **Chapter 9**, Unit 9.32 (2009).
2. Karatsoreos, I. N. *et al.* Endocrine and physiological changes in response to chronic corticosterone: a potential model of the metabolic syndrome in mouse. *Endocrinology* **151**, 2117–2127 (2010).
3. Moda-Sava, R. N. *et al.* Sustained rescue of prefrontal circuit dysfunction by antidepressant-induced spine formation. *Science* **364**, eaat8078 (2019).
4. Cui, Y. *et al.* Astroglial Kir4.1 in the lateral habenula drives neuronal bursts in depression. *Nature* **554**, 323–327 (2018).
5. Hao, Y. *et al.* Dictionary learning for integrative, multimodal and scalable single-cell analysis. *Nat Biotechnol* **42**, 293–304 (2024).
6. Love, M. I., Huber, W. & Anders, S. Moderated estimation of fold change and dispersion for RNA-seq data with DESeq2. *Genome Biol* **15**, 550 (2014).
7. Cerniauskas, I. *et al.* Chronic Stress Induces Activity, Synaptic, and Transcriptional Remodeling of the Lateral Habenula Associated with Deficits in Motivated Behaviors. *Neuron* **104**, 899–915.e8 (2019).
8. Hashikawa, Y. *et al.* Transcriptional and Spatial Resolution of Cell Types in the Mammalian Habenula. *Neuron* **106**, 743–758.e5 (2020).
9. Han, L. *et al.* Single-cell spatial transcriptomic atlas of the whole mouse brain. *Neuron* **113**, 2141–2160.e9 (2025).

Acknowledgements

We thank H. Ito, M. Diana, G.D. Stuber and all the members of the Mameli laboratory for comments on the manuscript. We thank the animal caregivers' team and L. Restivo of the Department of Fundamental Neuroscience for assistance. This work was supported by funds from the Canton of Vaud, the SNSF (310030_212193) and the State Secretariat for Education, Research and Innovation (SVEN) to M.M.

Author contributions

P.M. and M.M. conceptualized the project. P.M. conducted and analyzed behavioral experiments and performed in vivo two-photon calcium imaging with initial help of M.C. and S.M. P.M. prepared samples and quality assessment for spatial transcriptomics with the help of Q.A. and C.K.. D.O. supported P.M. in the analysis of two-photon data. J.G.C. and D.O. supported P.M. in the analysis of spatial transcriptomics. M.M. and P.M. wrote the manuscript with the help of all authors.

Competing interests

The authors declare no competing interests.

Additional information

Supplementary Information is available for this paper.

Correspondence and requests for materials should be addressed to Manuel Mameli.

Reprints and permissions information is available at www.nature.com/reprints.

Supplementary Files

This is a list of supplementary files associated with this preprint. Click to download.

- ExtendedDataTable1.csv
- ExtendedDataTable2.xlsx
- MolinaetalExtendedData.pdf